PHOTONICS Research

Broadband adiabatic polarization rotator-splitter based on a lithium niobate on insulator platform

Zhaoxi Chen,[1,†] Jingwei Yang,[1,†] Wing-Han Wong,[1] Edwin Yue-Bun Pun,[1,2] and Cheng Wang[1,2,*]

[1]Department of Electrical Engineering, City University of Hong Kong, Kowloon, Hong Kong, China
[2]State Key Laboratory of Terahertz and Millimeter Waves, City University of Hong Kong, Kowloon, Hong Kong, China
*Corresponding author: cwang257@cityu.edu.hk

Received 1 June 2021; revised 10 September 2021; accepted 21 September 2021; posted 29 September 2021 (Doc. ID 432906); published 8 November 2021

Polarization rotator-splitters (PRSs) are crucial components for controlling the polarization states of light in classical and quantum communication systems. We design and experimentally demonstrate a broadband PRS based on the lithium niobate on insulator (LNOI) platform. Both the rotator and splitter sections are based on adiabatically tapered waveguide structures, and the whole device only requires a single etching step. We show efficient PRS operation over an experimentally measured bandwidth of 130 nm at telecom wavelengths, potentially as wide as 500 nm according to simulation prediction, with relatively low polarization crosstalks of ~−10 dB. Our PRS is highly compatible with the design constraints and fabrication processes of common LNOI photonic devices, and it could become an important element in future LNOI photonic integrated circuits.

https://doi.org/10.1364/PRJ.432906

1. INTRODUCTION

Recent years have witnessed the rapid development of photonic devices in the lithium niobate on insulator (LNOI) platform, where strongly confined optical waveguides are formed in a submicrometer lithium niobate (LN) device layer on top of low-index substrates [1–3]. A wide range of high-performance photonic devices have been developed, including low-voltage and high-speed electro-optic modulators [4–6], efficient wavelength conversion devices [7,8], broadband frequency comb sources [9,10], as well as entangled photon pair generators [11,12]. Combining the excellent device performances with the commercial availability of LNOI wafers (up to 6 inches), photonic integrated circuits based on the LNOI platform are becoming a promising cost-effective solution for future optical communications systems in both the classical and quantum domains. Many of these systems make use of the polarization degree of freedom for information encoding and as a result are in need of devices that could efficiently perform tasks like polarization rotation and polarization splitting [13–17]. On the other hand, polarization manipulation devices are also important for processing incoming optical signals that do not possess a pure polarization state (e.g., from non-polarization-maintaining fibers).

A polarization rotator-splitter (PRS) is a promising solution that could address these demands. It is a compact device that can perform two polarization manipulation tasks, i.e., polarization rotation and polarization splitting, in one shot. A typical PRS splits two orthogonally polarized optical signals in the input port and separates them into different output ports while performing a 90° polarization rotation to one of the input signals as is schematically shown in Fig. 1(a). Reversing the input/output ports of a PRS effectively turns it into a polarization rotator-combiner due to reciprocity. Efficient PRSs have been realized in many popular integrated photonic platforms, including silicon (Si) [18–21], silicon nitride (SiN) [22], and indium phosphide (InP) [23]. These PRSs are mainly based on two strategies: mode coupling and mode evolution. The mode-coupling scheme typically features compact device footprints but is relatively narrowband and is more sensitive to fabrication variations [24]. On the other hand, mode-evolution-based PRSs require longer devices to fulfill the adiabatic evolution conditions, while exhibiting much wider operating bandwidths and better fabrication tolerance [21]. Most of these PRSs require a two-step etching process to create mode hybridization with sufficient coupling strength in rib-like waveguide structures [22,25,26]. More recently, computational inverse design methods have also been applied to realize ultracompact polarization manipulation devices in silicon-on-insulator (SOI) platforms [27–29]. In the LNOI platform, a polarization rotator has been demonstrated with plasmonic assisted waveguide structures [30], while PRSs have only been investigated theoretically so far [31–33]. Realization of broadband PRS could greatly expand the device toolbox of the LNOI platform.

In this work, we design and experimentally demonstrate a PRS in the LNOI platform, based on a two-stage adiabatic

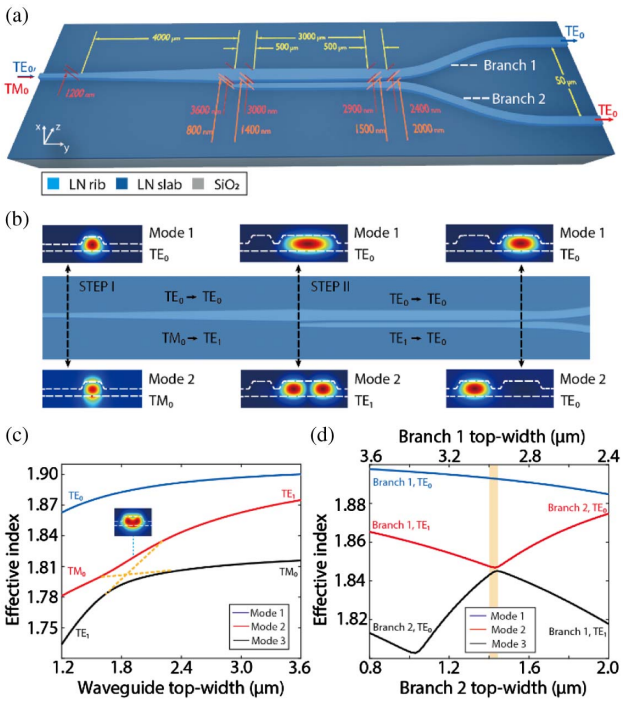

Fig. 1. (a) Schematic of the polarization rotator-splitter (PRS). In each taper section, the top widths of Branch 1 (Branch 2) are labeled in red (orange); lengths are labeled in yellow. (b) Optical eigenmode profiles (electric field intensity, viewed from the receiving end) at different locations along the PRS. Top (Mode 1) and bottom (Mode 2) profiles correspond to mode evolutions for TE_0 input and TM_0 input, respectively. (c), (d) Effective index (n_{eff}) evolution for the three lowest-order modes along the PRS in (c) Step I and (d) Step II, respectively, at the wavelength of 1550 nm. Inset of (c): optical intensity profile of the supermode at the avoided crossing between TM_0 and TE_1 modes in Step I.

mode evolution process. The device fabrication only requires a single etching step, and the resulting rib waveguide geometry is highly compatible with previously reported LNOI devices. The PRS shows a broad operation bandwidth from 1500 to 1630 nm (limited by our laser range), covering the entire telecom C- and L-bands and most of the S-band, with measured polarization crosstalks of ∼−8 dB and ∼−10 dB for the two output ports, respectively. Our numerical simulation results suggest that the operation bandwidths of our PRS could potentially be further extended to an ultrabroad range between 1300 and 1800 nm.

2. DEVICE DESIGN AND OPERATION PRINCIPLE

Figure 1(a) shows the schematic illustration of the on-chip PRS based on air-cladded LNOI waveguides. The PRS splits two input modes, namely, fundamental transverse-electric (TE_0) mode and fundamental transverse-magnetic (TM_0) mode, and it projects them separately into the TE_0 modes of the two output waveguide branches, respectively labeled as Branch 1 and Branch 2. The mode-evolution process in our PRS can be divided into two steps as shown in Fig. 1(b): an adiabatic polarization rotator (Step I) and an adiabatic mode splitter (Step II). Throughout the entire chip, a half-etched rib waveguide configuration is used, with a 250 nm rib height and a 250 nm slab thickness in an x-cut LN thin film as illustrated in the insets of Fig. 1(b). Both output modes of the proposed PRS are polarized along the crystal z axis of LN, which could readily make use of the largest $\chi^{(2)}$ tensor component (e.g., $r_{33} = 30$ pm/V), and are highly compatible with other electro-optic or nonlinear devices in LNOI.

In the polarization rotator (Step I), the LN rib waveguide adiabatically widens from a top width of 1.2 to 3.6 μm via a linear taper, such that the effective index of the second-order TE (TE_1) mode surpasses that of the fundamental TM (TM_0) mode [Fig. 1(c)]. The partially etched structure breaks the vertical symmetry of the waveguide and enables a substantial avoided crossing between the two modes ($\Delta n_{eff} = 0.019$) at a waveguide top width of 2.12 μm as shown in Fig. 1(c). As a result, the input TM_0 mode is converted first to a hybridized mode between TM_0 and TE_1 [inset of Fig. 1(c)] and finally to the TE_1 mode. While the input TM_0 mode is rotated and converted into TE_1 mode, the polarization state of the input TE_0 mode remains unchanged during Step I, since it stays the highest-index mode throughout the tapered structure [blue curve in Fig. 1(c)].

In Step II, an adiabatic coupler is designed to separate the TE_0 mode and TE_1 mode into different output channels. To achieve this, a side-branch waveguide (Branch 2) is placed next to the original waveguide (Branch 1) to extract the TE_1 mode and convert it into TE_0 mode in Branch 2, such that signals at both output ports are in TE_0 mode. Along the adiabatic coupler, Branch 1 gradually narrows while Branch 2 widens, such that the effective index of TE_1 mode in Branch 1 gradually drops below that of the TE_0 mode in Branch 2. The finite coupling between the two branches, in particular through the shared slab in between, again leads to an avoided crossing ($\Delta n_{eff} = 0.002$ for a waveguide top gap of 1000 nm) between the supermodes of the coupled-waveguide system as shown in Fig. 1(d). As a result, the energy of TE_1 mode in Branch 1 is gradually transferred to the TE_0 mode in Branch 2 following the red curve in Fig. 1(d), while the TE_0 mode in Branch 1 again remains decoupled [blue curve in Fig. 1(d)]. To ensure sufficient adiabaticity near the avoided crossing, we use a slower linear taper (top-width from 3.0 to 2.9 μm, over a length of 3000 μm) in the critical region [shaded area in Fig. 1(d)]. The waveguides before and after the middle stage are tapered by a relatively larger slope, such that the mode effective indices could be quickly pushed away from the avoided crossing points to minimize crosstalk between the two branches. Finally, the distance between the two output branches is gradually increased to 50 μm for testing.

Figures 2(a) and 2(b) show the numerically simulated electric field evolution along the PRS for TE_0 and TM_0 input, respectively, calculated using full 3D finite-difference time-domain (FDTD) simulation (Ansys Lumerical). To save the required computational power, the simulation uses a shortened device (1.5 mm in Step I and 1.2 mm in Step II) with a smaller coupling gap (top to top 450 nm) and a larger normal mode splitting ($\Delta n_{eff} = 0.0059$) in Step II. The product of taper

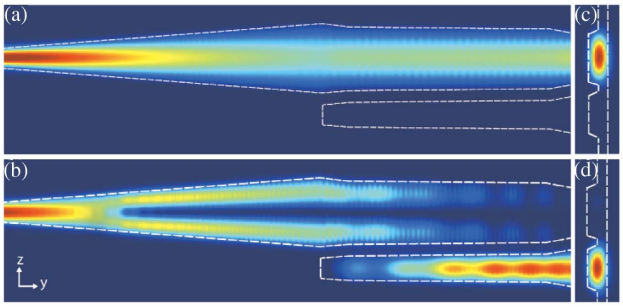

Fig. 2. (a), (b) Simulated electric field intensity evolution along the PRS for (a) TE_0 input and (b) TM_0 input at 1550 nm wavelength. Waveguide structure profiles are shown as white dashed lines. The y and z axes are not shown in the same scale for better viewing. (c), (d) Simulated electric field distributions (E_z) at the output facets of the Step II splitter for (c) TE_0 input and (d) TM_0 input.

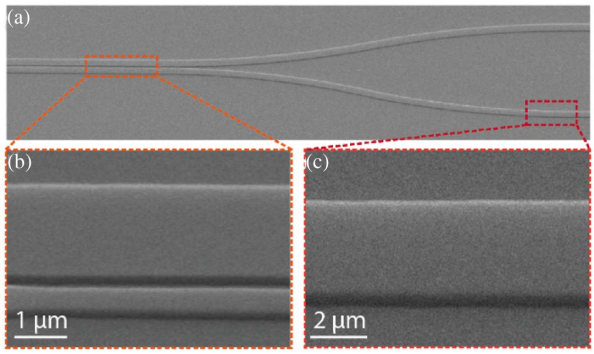

Fig. 3. Scanning electron microscope (SEM) images of (a) the polarization splitter (Step II) and the output bends, and the zoom-in views of (b) the adiabatic coupler and (c) the output straight waveguide.

length and $\Delta n_{\text{eff}} = 0.0059$ is kept consistent with the actual device to ensure the simulation captures a realistic taper adiabaticity. The simulated conversion efficiencies are 99.6% and 97.6% for TE_0 and TM_0 input [Figs. 2(c) and 2(d)], respectively, whereas the simulated polarization crosstalks are −16.2 dB and −23.9 dB for Port 1 and Port 2, respectively. TM_0 input light shows relatively lower conversion efficiency and higher crosstalk than TE_0 input, since it needs to go through two avoided crossings during the evolution process [Mode 2 in Figs. 1(c) and 1(d)], where the adiabatic conditions are harder to satisfy. The simulation results also suggest that the total device length of our PRS is largely dependent on the waveguide gap in Step II, currently limited by our fabrication process. Using a smaller waveguide gap (e.g., 450 nm used in simulation) could substantially increase the normal mode splitting at the avoided crossing, therefore reducing the taper length needed for an adiabatic mode transition. We estimate that the total device length could be reduced to ∼2 mm using a 450 nm gap without sacrificing device performance.

3. DEVICE FABRICATION AND CHARACTERIZATION

We fabricate the designed PRS using a commercial x-cut LNOI wafer (NANOLN) with an LN layer of 500 nm thick, a 2 μm buried silica layer, and a 500 μm silicon substrate. To define the waveguide structures, a 200 nm thick chromium (Cr) mask is first patterned through a sequence of electron-beam lithography (EBL), electron-beam evaporation, and standard lift-off processes [34]. The patterns are then transferred to the LN thin film by an argon ion (Ar^+)-based reactive ion etching (RIE) process. After removing the residual Cr mask, the chip facets are carefully polished for efficient fiber coupling and mode profile investigation. The total device length is 10 mm, including an 8 mm long PRS and two 1 mm straight sections on each side for fiber-to-chip coupling. The fabricated ridge waveguides feature an etch depth of ∼250 nm, consistent with the design parameters. Scanning electron microscope (SEM) images at various sections of the fabricated device are shown in Figs. 3(a)–3(c).

We first characterize the polarization splitting and rotation performances of our devices by directly imaging the optical mode profiles at the output facets of the PRS using a measurement setup shown in Fig. 4(a). Continuous-wave (CW) light from a broadband tunable telecom laser (Santec TSL-550, 1500–1630 nm) is launched to the input facet of the PRS through an SMF-28 lensed fiber with a focal spot size of 2 μm (OZ optics). A free-space fiber-bench polarization controller (FFBPC) is used to accurately control the input polarization state. At the output end, we directly image the optical profile using an objective lens focused at the chip facet and an infrared camera (Hamamatsu, C10366). A linear polarizer (LP) is used before the camera to examine the output optical profiles in specific polarization states (TE in the following experiments).

Using the direct imaging method, we show that our PRS could efficiently realize the designed polarization-control functions. To separately investigate the mode evolution performance in each section of our PRS, we fabricate and test two

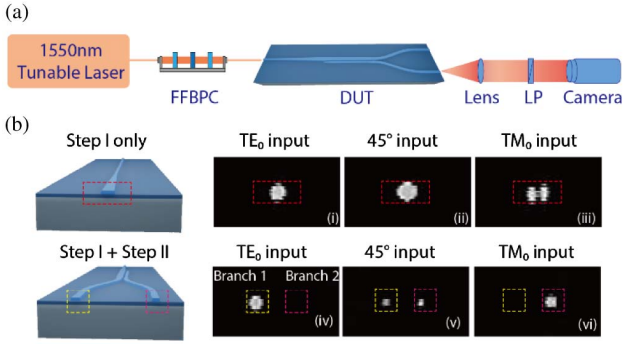

Fig. 4. (a) Experimental setup for output mode characterization. The free-space fiber-bench polarization controller (FFBPC) consists of a quarter-wave plate (QWP), a linear polarizer (LP), and a second QWP. (b) Infrared camera images of the mode profiles at the device output facet in cases of various input polarization states. The top row (i, ii, and iii) shows the output from a device with Step I only (objective lens NA = 0.45), while the bottom row (iv, v, and vi) shows the output from a full device with Step I + Step II (objective lens NA = 0.30).

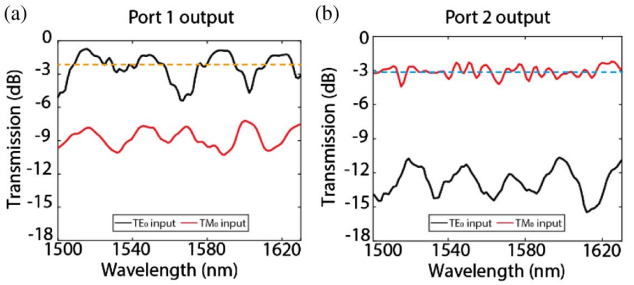

Fig. 5. Measured optical transmission spectra at the PRS output (a) Port 1 and (b) Port 2 in the wavelength range of 1500–1630 nm. Black and red curves correspond to TE_0 and TM_0 input polarizations, respectively.

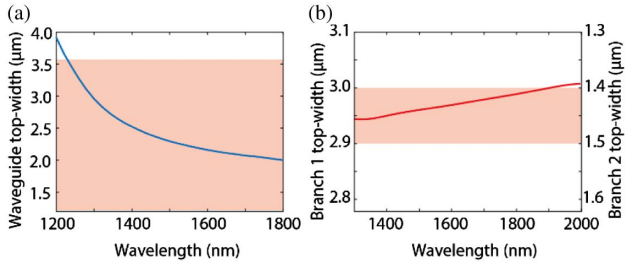

Fig. 6. Simulated mode hybridization points as functions of wavelength in (a) Step I rotator and (b) Step II splitter. The shaded area indicates the actual tapering regions in our device.

types of devices, i.e., devices with Step I only (converting TM_0 to TE_1) and devices with full PRS, the results of which are illustrated in the top and bottom rows of Fig. 4(b), respectively. For TE_0 input light, it remains in the initial polarization state and mode order (showing a single lobe) both after Step I only (i) and after the full PRS, and ultimately outputs from Branch 1 (Port 1) only (iv). On the other hand, the TM_0 input light first evolves into TE_1 mode in Step I, as indicated by the two-lobe output profile in (iii), and then sees a complete transfer to the fundamental TE_0 mode of Branch 2 (Port 2) after Step II (vi), consistent with our design. For comparison, we also investigated the PRS response when the input light is polarized at 45° with respect to pure TE/TM polarizations. Both at the end of Step I and the final output facet, the mode profiles could well correspond to superpositions of the output mode profiles upon pure TE_0 and TM_0 inputs.

To further quantitatively characterize the conversion efficiencies and polarization crosstalks of our PRS, we replace the objective lens at the output end with a second lensed fiber to collect the optical signals from a single output port at a time. The output optical powers for TE_0 and TM_0 input polarizations are respectively measured using an InGaAs photodetector for the entire laser tuning range of 1500–1630 nm as shown in Figs. 5(a) and 5(b). The data here correspond to on-chip optical transmissions, where a fiber-to-chip coupling loss of 6 dB/facet has been subtracted from the measured fiber-to-fiber transmission levels, consistent with our previous reports in a similar platform [35]. The average conversion efficiency from TE_0 input to Port 1 is ∼−2 dB, which is consistent with the estimated propagation loss of ∼2 dB/cm in our current LNOI platform (measured microresonator Q factor $\sim 2 \times 10^5$). The conversion efficiency from TM_0 input to Port 2 is slightly lower (∼−3 dB) than that of TE_0 input, since the input TM_0 mode as well as the intermediate TE_1 mode (in the Step I) experiences higher progation losses due to stronger interactions with the scattering centers on waveguide surfaces. Further improving the linear propagation loss to <0.1 dB/cm [36] could push the conversion efficiencies to >90% according to our simulation results. The measured crosstalk at Port 1 [Fig. 5(a)] is ∼−8 dB for the majority of tested wavelengths, except exhibiting degraded performance as much as 3–4 dB at a few specific wavelengths near 1500, 1565, and 1595 nm. The underperforming wavelengths could result from extra scattering losses due to fabrication imperfections in Branch 1, since there are no obvious transmission changes near these wavelengths in the output spectrum at Port 2. Fabrication-induced structural defects are likely also the limiting factor for the overall polarization crosstalk levels in the current devices. The output signal from Port 2 [Fig. 5(b)] shows almost flat responses over a broad wavelength range from 1500 to 1630 nm, with an average polarization crosstalk of ∼−10 dB from TE_0 input. The lower crosstalk for TE_0 input is also consistent with the numerical results discussed earlier. The crosstalks of our PRS could be further reduced by adopting a smaller coupling gap in Step II and improving the device fabrication process (e.g., increasing the waveguide sidewall verticality and reducing the surface roughness).

The measurement results confirm that our PRS design could well cover the entire C- and L-bands and majority of the S-band, limited only by the tuning range of our laser source, thanks to the adiabatic nature of these devices. The PRS performance could in principle be maintained as long as the mode hybridization point exists within the taper structure. Figure 6 shows the waveguide widths at which mode hybridization emerges, as functions of operating wavelength in Step I rotator and Step II splitter, respectively. The pink shades correspond to the actual taper range in Step I (from 1.2 to 3.6 μm) [Fig. 6(a)] and the critical taper range in the slowly tapering middle stage of Step II (Branch 1 tapering from 3.0 to 2.9 μm) [Fig. 6(b)]. The results in Fig. 6 indicate that Step I rotator could efficiently perform TM_0-to-TE_1 conversion for wavelengths from 1220 to 1800 nm, while Step II could well perform from 1300 to 1900 nm. Consequently, we estimate the operation band of the current PRS could potentially be as wide as 1300–1800 nm. Moreover, these devices do not include any resonant structures and therefore could process optical signals carrying high-speed data streams, ideally suited for polarization-division multiplexed LN photonic integrated circuits.

4. CONCLUSIONS

In conclusion, we design and experimentally demonstrate an adiabatic PRS based on the LNOI platform, achieved by a single etching step. We show polarization crosstalk of ∼−8 dB at Port 1 and ∼−10 dB at Port 2 for the majority of measured wavelengths over a broad spectral range from 1500 to 1630 nm. The adiabatic nature of these devices suggests that they could potentially operate at an ultrabroad bandwidth of ∼500 nm.

We estimate that the total device length can be further reduced to <2 mm by narrowing the waveguide gap, adopting a more asymmetric waveguide cross section, and increasing the waveguide sidewall angle, and possibly to <200 μm using directional couplers instead of adiabatic tapers (with trade-off in bandwidth). Importantly, the fabrication process, waveguide geometry, crystal orientation, and input/output optical modes used in our PRS are highly compatible with other functional photonic devices reported in the LNOI platform. Further integrating these PRSs with other active components like high-speed electro-optical modulators could enable fully integrated dual-polarization photonic integrated circuits for future optical signal transmission and information processing systems.

Funding. National Natural Science Foundation of China (61922092); Research Grants Council, University Grants Committee (CityU 11210317, CityU 21208219); City University of Hong Kong (9610402, 9610455).

Acknowledgment. We thank Mr. Ke Zhang, Dr. Wenzhao Sun, and Mr. Hanke Feng for their help in device fabrication and SEM imaging, and we thank Dr. Di Zhu for helpful discussions.

Disclosures. The authors declare no conflicts of interest.

Data Availability. Data underlying the results presented in this paper are not publicly available at this time but may be obtained from the authors upon reasonable request.

†These authors contributed equally to this paper.

REFERENCES

1. A. Boes, B. Corcoran, L. Chang, J. Bowers, and A. Mitchell, "Status and potential of lithium niobate on insulator (LNOI) for photonic integrated circuits," Laser Photon. Rev. **12**, 1700256 (2018).
2. D. Zhu, L. Shao, M. Yu, R. Cheng, B. Desiatov, C. J. Xin, Y. Hu, J. Holzgrafe, S. Ghosh, A. Shams-Ansari, E. Puma, N. Sinclair, C. Reimer, M. Zhang, and M. Lončar, "Integrated photonics on thin-film lithium niobate," Adv. Opt. Photon. **13**, 242–352 (2021).
3. J. Lin, F. Bo, Y. Cheng, and J. Xu, "Advances in on-chip photonic devices based on lithium niobate on insulator," Photon. Res. **8**, 1910–1936 (2020).
4. C. Wang, M. Zhang, X. Chen, M. Bertrand, A. Shams-Ansari, S. Chandrasekhar, P. Winzer, and M. Loncar, "Integrated lithium niobate electro-optic modulators operating at CMOS-compatible voltages," Nature **562**, 101–104 (2018).
5. M. Xu, M. He, H. Zhang, J. Jian, Y. Pan, X. Liu, L. Chen, X. Meng, H. Chen, Z. Li, X. Xiao, S. Yu, S. Yu, and X. Cai, "High-performance coherent optical modulators based on thin-film lithium niobate platform," Nat. Commun. **11**, 3911 (2020).
6. P. Kharel, C. Reimer, K. Luke, L. He, and M. Zhang, "Breaking voltage–bandwidth limits in integrated lithium niobate modulators using micro-structured electrodes," Optica **8**, 357–363 (2021).
7. C. Wang, C. Langrock, A. Marandi, M. Jankowski, M. Zhang, B. Desiatov, M. M. Fejer, and M. Lončar, "Ultrahigh-efficiency wavelength conversion in nanophotonic periodically poled lithium niobate waveguides," Optica **5**, 1438–1441 (2018).
8. J. Lu, J. B. Surya, X. Liu, A. W. Bruch, Z. Gong, Y. Xu, and H. X. Tang, "Periodically poled thin-film lithium niobate microring resonators with a second-harmonic generation efficiency of 250,000%/W," Optica **6**, 1455–1460 (2019).
9. M. Zhang, B. Buscaino, C. Wang, A. Shams-Ansari, C. Reimer, R. Zhu, J. M. Kahn, and M. Loncar, "Broadband electro-optic frequency comb generation in a lithium niobate microring resonator," Nature **568**, 373–377 (2019).
10. Y. He, Q.-F. Yang, J. Ling, R. Luo, H. Liang, M. Li, B. Shen, H. Wang, K. Vahala, and Q. Lin, "Self-starting bi-chromatic $LiNbO_3$ soliton microcomb," Optica **6**, 1138–1144 (2019).
11. J. Zhao, C. Ma, M. Rusing, and S. Mookherjea, "High quality entangled photon pair generation in periodically poled thin-film lithium niobate waveguides," Phys. Rev. Lett. **124**, 163603 (2020).
12. B. S. Elkus, K. Abdelsalam, A. Rao, V. Velev, S. Fathpour, P. Kumar, and G. S. Kanter, "Generation of broadband correlated photon-pairs in short thin-film lithium-niobate waveguides," Opt. Express **27**, 38521–38531 (2019).
13. D. Dai, C. Li, S. Wang, H. Wu, Y. Shi, Z. Wu, S. Gao, T. Dai, H. Yu, and H.-K. Tsang, "10-channel mode (de)multiplexer with dual polarizations," Laser Photon. Rev. **12**, 1700109 (2018).
14. C. Ma, W. D. Sacher, Z. Tang, J. C. Mikkelsen, Y. Yang, F. Xu, T. Thiessen, H.-K. Lo, and J. K. S. Poon, "Silicon photonic transmitter for polarization-encoded quantum key distribution," Optica **3**, 1274–1278 (2016).
15. H. P. Chung, C. H. Lee, K. H. Huang, S. L. Yang, K. Wang, A. S. Solntsev, A. A. Sukhorukov, F. Setzpfandt, and Y. H. Chen, "Broadband on-chip polarization mode splitters in lithium niobate integrated adiabatic couplers," Opt. Express **27**, 1632–1645 (2019).
16. C. Sun, Y. Yu, Y. Ding, Z. Li, W. Qi, and X. Zhang, "Integrated mode-transparent polarization beam splitter supporting thirteen data channels," Photon. Res. **8**, 978–985 (2020).
17. D. González-Andrade, C. Lafforgue, E. Durán-Valdeiglesias, X. Le Roux, M. Berciano, E. Cassan, D. Marris-Morini, A. V. Velasco, P. Cheben, and L. Vivien, "Polarization-and wavelength-agnostic nanophotonic beam splitter," Sci. Rep. **9**, 3604 (2019).
18. D. Dai and J. E. Bowers, "Novel concept for ultracompact polarization splitter-rotator based on silicon nanowires," Opt. Express **19**, 10940–10949 (2011).
19. D. Dai, Y. Tang, and J. E. Bowers, "Mode conversion in tapered submicron silicon ridge optical waveguides," Opt. Express **20**, 13425–13439 (2012).
20. D. Dai, L. Liu, S. Gao, D.-X. Xu, and S. He, "Polarization management for silicon photonic integrated circuits," Laser Photon. Rev. **7**, 303–328 (2013).
21. W. D. Sacher, T. Barwicz, B. J. Taylor, and J. K. Poon, "Polarization rotator-splitters in standard active silicon photonics platforms," Opt. Express **22**, 3777–3786 (2014).
22. W. D. Sacher, Y. Huang, L. Ding, T. Barwicz, J. C. Mikkelsen, B. J. Taylor, G. Q. Lo, and J. K. Poon, "Polarization rotator-splitters and controllers in a Si_3N_4-on-SOI integrated photonics platform," Opt. Express **22**, 11167–11174 (2014).
23. C.-J. Chung, J. Midkiff, K. M. Yoo, A. Rostamian, J. Guo, R. T. Chen, and S. Chakravarty, "InP-based polarization rotator-splitter for mid-infrared photonic integration circuits," AIP Adv. **9**, 015303 (2019).
24. H. Guan, A. Novack, M. Streshinsky, R. Shi, Q. Fang, A. E. Lim, G. Q. Lo, T. Baehr-Jones, and M. Hochberg, "CMOS-compatible highly efficient polarization splitter and rotator based on a double-etched directional coupler," Opt. Express **22**, 2489–2496 (2014).
25. Y. Xiong, D. X. Xu, J. H. Schmid, P. Cheben, S. Janz, and W. N. Ye, "Fabrication tolerant and broadband polarization splitter and rotator based on a taper-etched directional coupler," Opt. Express **22**, 17458–17465 (2014).
26. K. Tan, Y. Huang, G. Q. Lo, C. Lee, and C. Yu, "Compact highly-efficient polarization splitter and rotator based on 90 degrees bends," Opt. Express **24**, 14506–14512 (2016).
27. S. Molesky, Z. Lin, A. Y. Piggott, W. Jin, J. Vucković, and A. W. Rodriguez, "Inverse design in nanophotonics," Nat. Photonics **12**, 659–670 (2018).
28. W. Chang, S. Xu, M. Cheng, D. Liu, and M. Zhang, "Inverse design of a single-step-etched ultracompact silicon polarization rotator," Opt. Express **28**, 28343–28351 (2020).
29. B. Shen, P. Wang, R. Polson, and R. Menon, "An integrated-nanophotonics polarization beamsplitter with 2.4×2.4 μm^2 footprint," Nat. Photonics **9**, 378–382 (2015).

30. Y. Zhao, W. Yu, S. Dai, J. Li, T. Lin, M. Li, and J. Liu, "Compact lithium-niobate-on-insulator polarization rotator based on asymmetric hybrid plasmonics waveguide," IEEE Photon. J. **13**, 4800105 (2021).
31. Z. Y. Chen, Y. Pan, X. Y. Liu, H. T. Lin, X. M. Zhong, and X. L. Cai, "Single-step etching polarization splitter-rotator based on lithium niobate ridge waveguide," in *Asia Communications and Photonics Conference* (Optical Society of America, 2019), paper M4A-285.
32. L. Zhang, L. Zhang, X. Fu, and L. Yang, "Compact, broadband and low-loss polarization beam splitter on lithium-niobate-on-insulator using a silicon nanowire assisted waveguide," IEEE Photon. J. **12**, 6601906 (2020).
33. A. Pan, C. Hu, C. Zeng, and J. Xia, "Fundamental mode hybridization in a thin film lithium niobate ridge waveguide," Opt. Express **27**, 35659–35669 (2019).
34. K. Zhang, Z. Chen, H. Feng, W. H. Wong, E. Y. B. Pun, and C. Wang, "High-*Q* lithium niobate microring resonators using lift-off metallic masks," Chin. Opt. Lett. **19**, 060010 (2021).
35. Z. Chen, Q. Xu, K. Zhang, W. H. Wong, D. L. Zhang, E. Y. B. Pun, and C. Wang, "Efficient erbium-doped thin-film lithium niobate waveguide amplifiers," Opt. Lett. **46**, 1161–1164 (2021).
36. M. Zhang, C. Wang, R. Cheng, A. Shams-Ansari, and M. Lončar, "Monolithic ultra-high-*Q* lithium niobate microring resonator," Optica **4**, 1536–1537 (2017).